

Warm gas in the vicinity of a supermassive black hole 13 billion years ago

Received: 17 June 2024

Accepted: 11 February 2025

Published online: 07 March 2025



K. Tadaki^{1,2}✉, F. Esposito^{3,4}, L. Vallini⁴, T. Tsukui^{5,6}, T. Saito⁷, D. Iono^{2,8} & T. Michiyama⁹

Quasars, powered by supermassive black holes, are among the brightest objects in the Universe. In the vicinity of a supermassive black hole, X-ray photons from an active galactic nucleus can heat the surrounding gas to several hundred kelvin. Here we report observations of dust continuum and carbon monoxide (CO) $J = 13-12$ and $J = 14-13$ line emissions at a resolution of 130 pc in a luminous quasar at a redshift of 6. We successfully detected these high- J CO line emissions from warm gas in a compact disk component. The CO luminosity ratio in the central region of the compact disk is consistent with theoretical models in which X-ray heating dominates the CO excitation and the gas column density is as high as 10^{25} cm^{-2} . This finding demonstrates that high-resolution observations of high- J CO lines are promising ways to identify extremely dust-obscured quasars in the early Universe.

In the Universe at a redshift (z) > 6 , corresponding to 13 billion years ago, luminous quasars containing a supermassive black hole (SMBH) with a mass exceeding $10^9 M_\odot$ have been discovered^{1–4}. Many of these quasars were originally identified by wide-field surveys at optical and near-infrared wavelengths and were subsequently detected at submillimetre wavelengths, with some reaching total infrared luminosities of $L_{\text{IR}} = 10^{13} L_\odot$ (refs. 5,6). Studying the interstellar medium surrounding an active galactic nucleus (AGN) in such luminous quasars is crucial to understanding the interaction between an AGN and its surrounding environment. Rotational–vibrational excitation lines of molecular hydrogen in the near infrared are useful for tracing warm (1,000–2,000 K) molecular gas directly affected by an AGN⁷. However, it is difficult to observe these emission lines in the central regions of distant quasars owing to sensitivity and spatial resolution limitations, even with the James Webb Space Telescope. Observations of highly excited rotational transitions of carbon monoxide (high- J CO lines) are an alternative approach to probe warm gas in quasars^{8–11}. Previous observations of high- J CO lines had low spatial resolution and could not constrain the location of the warm gas and its heating mechanism.

The scope of this Article is to understand the relationship between warm gas and AGN in the central regions of quasars in the early Universe.

Results

ALMA observations

To directly probe the warm gas in the vicinity of an AGN, we observed CO $J = 13-12$ and CO $J = 14-13$ lines with upper energy levels of $E_u/k_B = 500-600 \text{ K}$, as well as dust continuum emission, in J231038.88+185519.7 (hereafter J2310+1855) at $z = 6.00$ with a high spatial resolution of 130 pc (0.022 arcsec) using the Atacama Large Millimeter/submillimeter Array (ALMA) (Extended Data Table 1). J2310+1855 is one of the brightest quasars in both optical and submillimeter emission^{6,12}. The detection of a broad MgII emission line extending over $3,000 \text{ km s}^{-1}$ implies a SMBH with a mass of $M_{\text{BH}} = (2-4) \times 10^9 M_\odot$ in the centre of J2310+1855 (ref. 13) (Extended Data Fig. 1). Figure 1a shows the ALMA image of the 1.4-mm continuum emission at a resolution of 130 pc (Extended Data Table 2). We found that the dust emission comes from a compact disk with an effective radius of $R_e = 266 \pm 14 \text{ pc}$ (Methods and Extended Data Fig. 2). Such a centrally concentrated gas disk may have been formed by

¹Faculty of Engineering, Hokkai-Gakuen University, Sapporo, Japan. ²National Astronomical Observatory of Japan, Mitaka, Japan. ³Dipartimento di Fisica e Astronomia, Università degli Studi di Bologna, Bologna, Italy. ⁴Osservatorio di Astrofisica e Scienza dello Spazio (INAF–OAS), Bologna, Italy. ⁵Research School of Astronomy and Astrophysics, Australian National University, Canberra, Australian Capital Territory, Australia. ⁶ARC Centre of Excellence for All Sky Astrophysics in 3 Dimensions (ASTRO 3D), Canberra, Australian Capital Territory, Australia. ⁷Faculty of Global Interdisciplinary Science and Innovation, Shizuoka University, Shizuoka, Japan. ⁸Department of Astronomical Science, The Graduate University for Advanced Studies (SOKENDAI), Mitaka, Japan. ⁹Faculty of Information Science, Shunan University, Shunan, Japan. ✉e-mail: tadaki@hgu.jp

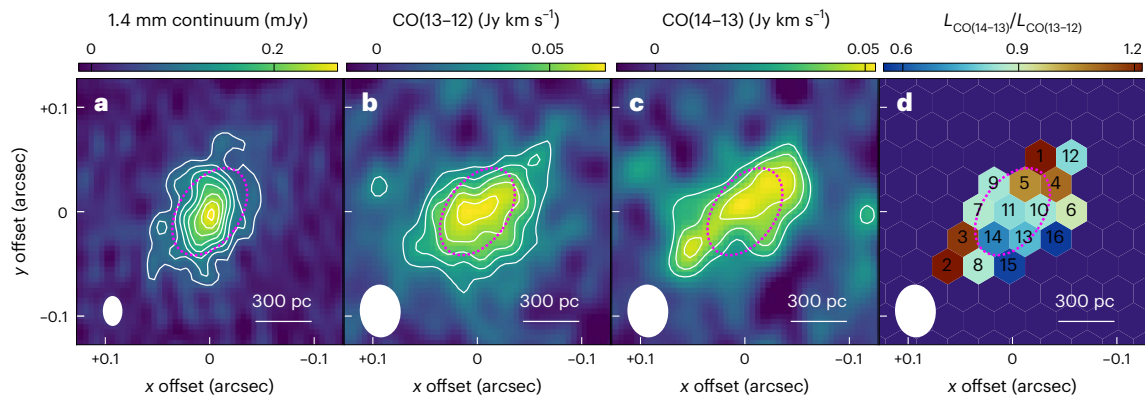


Fig. 1 | Morphology of a luminous quasar at $z = 6.0$, J2310+1855. a–d, ALMA maps of 1.4-mm continuum (a), CO $J = 13-12$ emission (b), CO $J = 14-13$ emission (c) and CO luminosity ratio (d). The contours are plotted every 1σ from 3σ in a and b and every 2σ from 5σ in c, where 1σ is the RMS of each image. The angular

resolution is $0.029'' \times 0.019''$ (a position angle of 0.5°) for the continuum and $0.051'' \times 0.039''$ (3.1°) for the CO maps. The dashed magenta line shows the effective radius of the compact disk ($R_e = 266$ pc).

efficient gas transport driven by a major merger^{14,15}, and its detection has been reported in other luminous quasars at $z \approx 6-7$ (refs. 16–19). High-resolution observations of [CII] line emission, which traces cold gas, have been used extensively to study the distribution of molecular gas masses and black hole masses in the central compact disk of quasars^{17,18}. By contrast, warm gas at these spatial scales has received comparatively little attention and remains largely unexplored. We have now detected the CO $J = 13-12$ and CO $J = 14-13$ emissions in the central compact disk using ALMA images with 250 pc resolution (Fig. 1b,c).

Near an AGN, X-rays from an accretion disk and its associated coronal gas are expected to heat the molecular gas to high temperatures, resulting in bright high- J CO line emission. This is in contrast to star-forming regions, where cold gas dominates. Even higher- J CO emission has been detected in other quasars at $z > 6$ (refs. 8,11), suggesting a strong contribution from X-ray-dominated regions (XDRs). In the nearest quasar, Mrk 231, at $z = 0.04$, a CO $J = 13-12$ line emission has been detected by the Herschel Space Observatory²⁰. However, due to the low spatial resolution of 15 kpc, there is still no direct evidence that the high- J CO emission is associated with warm gas in the vicinity of an AGN. High- J CO lines from high-redshift quasars are shifted to wavelengths with good atmospheric transmission (1–2 mm) and can be observed with large ground-based telescopes that provide high-spatial-resolution data. Our high-resolution ALMA images directly indicate the presence of warm gas in the central region where an AGN is expected to be located.

Comparisons with theoretical models

The observed luminosity ratios of CO $J = 14-13$ and CO $J = 13-12$ emissions are within the range of $L_{\text{CO}(14-13)}/L_{\text{CO}(13-12)} = 0.5-1.4$ (Fig. 1d). We then identify the primary heating source of the warm gas by comparing the CO ratios with theoretical models that consider three physical mechanisms: heating associated with star formation activity in photo-dissociation regions (PDRs), heating associated with black holes in XDRs and heating associated with shock waves. Previous Herschel observations have shown that the luminosity ratios of galaxy-integrated CO line emission do not necessarily provide an accurate classification of the heating mechanisms in the interstellar medium²¹. For example, although the nearby ULIRG NGC 6240 has a CO spectral line energy distribution (SLED) similar to that of Mrk 231, its detailed studies suggest that the gas is heated by shocks²². We address this issue of the heating mechanism by comparing gas and dust data at smaller spatial scales, which are not available from observations of nearby galaxies, with physically motivated models^{23,24} (Methods).

In the PDR models, where far-ultraviolet (6–13.6 eV) photons from massive OB-type stars regulate the heating and ionization of the

gas, CO ratios increase with star formation rates (SFRs). The total SFR of J2310+1855 is $1,000-3,000 M_\odot \text{ yr}^{-1}$, including the host galaxy^{25,26}. Even taking into account the extreme stellar radiation, which is 10^6 times larger than the far-ultraviolet radiation field in the Milky Way ($G_0 = 10^6$), the CO ratios above 0.5 cannot be explained by the PDR model (Fig. 2). In theory, high- J /CO emission can be excited even in PDRs if the gas disk consists entirely of clumps with densities of 10^6 cm^{-3} (ref. 27). However, because such high-density regions are expected to have a low volume filling factor, our model assumes a log-normal distribution of the gas densities of clumps²⁸. Observations of local AGN host galaxies also support that PDRs contribute little to the excitation of such high- J CO emission lines^{24,29}.

Next, we consider the XDR heating. Because J2310+1855 is detected in X-rays with a luminosity of $L_{2-10\text{keV}} = 6.9 \times 10^{44} \text{ erg s}^{-1}$ (ref. 30), it is reasonable to assume that the central X-ray source has a strong influence on the excitation conditions of the molecular gas in the central region. We assume that the gas in the compact disk with $R_e = 266$ pc is primarily responsible for the attenuation of the X-ray emission from an AGN. In regions radially away from the centre, the gas column density accumulated along the radial direction increases, leading to a rapid decrease in the incident X-ray flux due to a shielding effect (Extended Data Fig. 3). We compare the observed luminosity ratios of the CO $J = 14-13$ and CO $J = 13-12$ emissions with those in the XDR models of the compact disk with gas column densities of $N_{\text{H}} = 10^{24.5-25.5} \text{ cm}^{-2}$ at a galactocentric radius of 1 kpc (Fig. 2). The XDR models with larger column densities have smaller CO ratios at the same radius. The XDR models then reasonably explain a high CO ratio of $L_{\text{CO}(14-13)}/L_{\text{CO}(13-12)} \approx 0.8$ at radii of $R < 200$ pc and a decreasing trend to a lower $L_{\text{CO}(14-13)}/L_{\text{CO}(13-12)} \approx 0.5$ in the southwestern region (Fig. 1d, ID 15–16). Note that the gas column density here is measured in the radial direction of the compact disk, not in the line of sight. X-ray observations of several high- z quasars, including J2310+1855, suggest that the gas column density in the line-of-sight direction is typically $N_{\text{H}} < 9 \times 10^{22} \text{ cm}^{-2}$ (ref. 30), which is much smaller than what we consider.

In the northwestern and southeastern regions of the compact disk (Fig. 1d, ID 1–4), the CO $J = 14-13$ emission is almost thermalized ($L_{\text{CO}(14-13)}/L_{\text{CO}(13-12)} \approx 1.25$) and cannot be explained by either the PDR or the XDR model. We consider the possibility of mechanical heating by shocks. Powerful outflows are often detected in luminous quasars^{31,32}. The interaction of quasar-driven outflows with the surrounding gas is expected to produce a shock wave that heats the gas to a high temperature. If the direction of bipolar outflows is inclined relative to a disk plane, the shock heating would affect gas in regions slightly away from the centre. We use a planar shock model^{33,34} to predict CO fluxes in the large velocity gradient approximation. The model calculates temperature

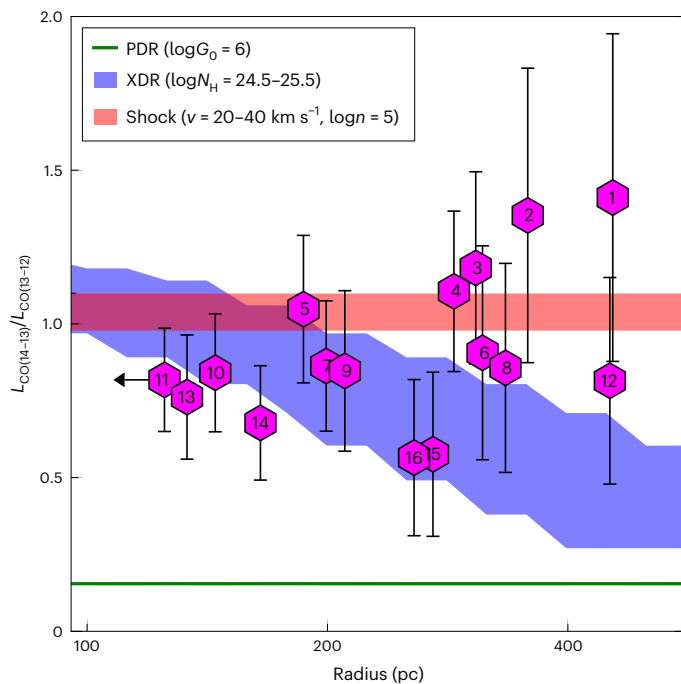


Fig. 2 | A variation of luminosity ratio between CO $J = 14-13$ and CO $J = 13-12$ emissions at different galactocentric radii. The magenta hexagons denote the CO ratios determined from ALMA observations, corresponding to the IDs used in Fig. 1d. The error bars represent 1σ uncertainties of the flux measurements. Theoretical model comparisons are shown with a green line representing PDR models with $G_0 = 10^6$, the blue-shaded regions represent XDR models with gas column densities ranging from $N_{\text{H}} = 10^{24.5} \text{ cm}^{-2}$ (upper bound) to $N_{\text{H}} = 10^{25.5} \text{ cm}^{-2}$ (lower bound) and the red-shaded regions represent shock models with velocities ranging from $v = 20 \text{ km s}^{-1}$ (lower bound) to $v = 40 \text{ km s}^{-1}$ (upper bound) and a gas density of $n = 10^5 \text{ cm}^{-3}$.

and density profiles taking into account several processes: gas-grain interactions, grain charge variation and momentum transfer between charged and neutral fluids. CO excitation depends on a shock velocity and a gas density of the preshock gas. The shock model with a velocity of $v = 20-40 \text{ km s}^{-1}$ and a density of $n = 10^5 \text{ cm}^{-3}$ explains a high CO ratio of $L_{\text{CO}(14-13)}/L_{\text{CO}(13-12)} = 1.0-1.1$, independent of galactocentric radii.

Because the gas in the central region can be excited by either XDR or shocks, it is difficult to distinguish between the two mechanisms on the basis of the CO ratios alone. Therefore, we use the dust information from the ALMA observations. An AGN produces ultraviolet continuum emission as well as X-rays and efficiently heats the dust. In the nuclear region ($<200 \text{ pc}$) of Mrk 231, the dust emission is likely to be dominated by a warm (100 K) component, rather than a cold (40 K) component³⁵, supporting dust heating by an AGN. By contrast, shocks do not affect dust, while gas is compressed and heated to higher temperatures²². We detected multiwavelength continuum emission in J2310+1855 with a resolution of 460 pc (0.08 arcsec) and with a resolution of 1.4 kpc (0.24 arcsec) (Extended Data Fig. 4 and Extended Data Table 3). By characterizing the spatially resolved spectral energy distributions (SEDs) of the dust emission (Fig. 3, left), we find that the dust temperature is $T_{\text{d}} = 74^{+7}_{-5} \text{ K}$ in the central region (within a radius of 230 pc) and $T_{\text{d}} = 59^{+4}_{-4} \text{ K}$ in the extended region (within a radius of 700 pc), which is consistent with a previous study³⁶. In a quasar at $z = 4.4$, the dust temperature has been reported to increase towards smaller galactocentric radii, reaching up to 60–70 K within the central 500 pc (ref. 37). Furthermore, in the central 110-pc region of a quasar at $z = 6.9$, the dust temperature is even higher, exceeding 132 K (ref. 17). Because shocks do not heat the dust, measuring the dust temperature in the small

central regions of quasars using high-spatial-resolution observations is a powerful way to prove that the dust and gas are being heated by the AGN. The higher dust temperature in the central region supports the scenario that the gas in the central region is heated by XDR rather than by shocks.

In addition to the CO $J = 13-12$ and CO $J = 14-13$ lines, we detected CO $J = 6-5$ and CO $J = 8-7$ emission lines with an upper energy level of $E_{\text{u}}/k_{\text{B}} = 100-200 \text{ K}$ at a spatial resolution of 460 pc (Extended Data Fig. 5 and Extended Data Table 3). A CO SLED including mid- J CO lines is helpful for understanding the heating mechanism acting on molecular gas. Here, we consider the effect of dust attenuation on CO SLEDs. The multiwavelength analysis of the dust SED shows that the optical depth of the dust emission is unity at the rest-frame wavelength of $\lambda_0 = 266^{+52}_{-49} \mu\text{m}$ in the central region (Fig. 3, left). In interstellar medium (ISM) where gas and dust are well mixed, emissions at the shorter wavelengths, such as CO $J = 13-12$ ($\lambda = 200 \mu\text{m}$) and CO $J = 14-13$ ($\lambda = 186 \mu\text{m}$) lines, can be attenuated by dust³⁸. We therefore correct the CO line fluxes for dust attenuation. The corrected CO SLED in the central region peaks at $J \geq 9$, while the galaxy-integrated one peaks at $J = 8$ (ref. 10) (Fig. 3, right). This radial gradient of the CO excitation supports the scenario that the XDR heating preferentially works in the central region. We integrated the XDR model out to a radius of 230 pc to compute a CO SLED normalized at $J = 13$. The XDR model is broadly consistent with the CO SLED in the central region. Meanwhile, the observations indicate that the CO lines are still highly excited in the outer region at galactocentric radii of $R = 230-700 \text{ pc}$, where the X-ray emission is attenuated by gas in the compact disk. Because neither PDR nor XDR can reproduce such a CO SLED, shocks are probably responsible for the CO excitation in the outer region as well as in the northwestern and southeastern regions of the compact disk (Fig. 1d, ID 1–4).

Spatial extent of outflowing gas

We search for signatures of outflows in J2310+1855 based on ALMA observations of ionized carbon ([CII]) emission to explore the physical origins of shocks. We use all archival data to obtain a deep spectrum of [CII] emission with a spatial resolution of 8 kpc (Fig. 4). The spectrum of the whole galaxy is well characterized by two Gaussian components (Fig. 4, top), which can be interpreted as gas in the rotating disk of the host galaxy. Previous studies of the gas kinematics of this quasar report a rotation velocity of 150–180 km s^{-1} before inclination correction^{36,39}. After subtracting the disk component, we find excess emission at the 5σ level, where 1σ denotes the noise level in the ALMA cube, in four continuous bins in the velocity range of $-465 \text{ km s}^{-1} < v < -345 \text{ km s}^{-1}$ (Fig. 4, bottom). Such a high-velocity wing component is independent of the rotating disk of the host galaxy and is likely to be an outflow component. The [CII] flux of the blue wing component is $0.092 \pm 0.011 \text{ Jy km s}^{-1}$, in broad agreement with a previous study²⁶. Assuming a circular Gaussian profile, we find that the wing component has a circularized effective radius of $R_{\text{e,circ}} = 2.4 \pm 0.4 \text{ kpc}$ from the visibility fit to all data in the ALMA archive (Methods and Extended Data Fig. 6). Meanwhile, the disk component in the velocity range from -315 km s^{-1} to $+315 \text{ km s}^{-1}$ has $R_{\text{e,circ}} = 1.3 \pm 0.1 \text{ kpc}$. Our size measurements indicate that the [CII] emission of the wing component is distributed throughout the galaxy disk. The gas in the outer region could be highly excited by shocks generated by the interaction of the galaxy-scale outflow with the gas in the compact disk. Such interactions have also been suggested in a nearby AGN⁴⁰ and a high-redshift quasar⁴¹.

Discussion

An approach to searching for dust-obscured quasars

Figure 5 shows the geometric configuration of the two disks and outflow components of J2310+1855 as inferred from the ALMA observations. Independent analyses of [CII] kinematics show that a gas disk is inclined by about 40° (refs. 36,39). This is consistent with the large difference

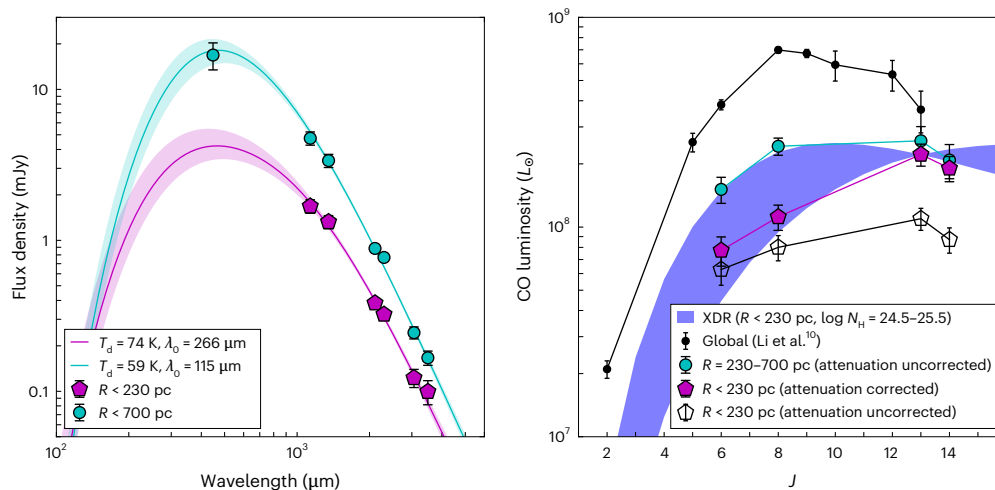


Fig. 3 | Energy distributions of dust continuum and CO line emissions in J2310+1855. Left: dust SEDs in areas inside a radius of 230 pc (magenta pentagons) and inside a radius of 700 pc (cyan circles). The error bars represent 1σ uncertainties of the flux measurements. The magenta and cyan lines indicate the best-fit models of modified blackbody radiation with $T_d = 74$ K and $T_d = 59$ K, respectively. The shaded regions in magenta and cyan denote 1σ uncertainties associated with these models. Right: pentagons, cyan circles and black circles

represent CO SLEDs in the central region ($R < 230$ pc), in the outer region ($R = 230$ –700 pc) and in the whole region¹⁰, respectively. The magenta pentagons show attenuation-corrected CO luminosities, while open pentagons show uncorrected luminosities. The error bars represent 1σ uncertainties of the flux measurements. The blue-shaded region corresponds to the XDR model with gas column densities ranging from $N_H = 10^{24.5} \text{ cm}^{-2}$ (lower bound at $J < 13$, upper bound at $J > 13$) to $N_H = 10^{25.5} \text{ cm}^{-2}$ (upper bound at $J < 13$, lower bound at $J > 13$).

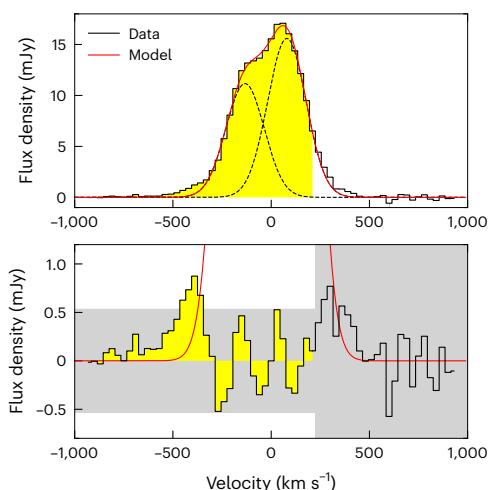


Fig. 4 | [CII] spectrum in J2310+1855. Top: the solid black line shows the spectrum extracted from the $1.5''$ -resolution cube. One of the archival data points (2019.1.01721.S) does not cover the velocity range of $v > +225 \text{ km s}^{-1}$, which is not highlighted by yellow. The red curve represents the best-fit model, which consists of two Gaussian components shown as dashed lines, in a velocity range of $v < +225 \text{ km s}^{-1}$. Bottom: we obtained the residual spectrum by subtracting the best-fit model from the observed spectrum. The grey-shaded region corresponds to the 5σ level in the cube.

between the column density in the line of sight estimated from X-ray observations ($N_H < 9 \times 10^{22} \text{ cm}^{-2}$)³⁰ and the column density in the radial direction of the compact disk estimated from the CO line ratio measurements ($N_H \approx 10^{25} \text{ cm}^{-2}$). If the compact disk were observed from the radial direction, J2310+1855 would be classified as an extremely dust-obscured quasar with $N_H \approx 10^{25} \text{ cm}^{-2}$ and would be missed in optical and X-ray observations. One of the scenarios for the growth of SMBHs is that gas-rich galaxies collide and merge, leading to an active phase of dusty star formation and a dusty AGN⁴². During this phase, an SMBH is fed by gas at the galactic centre. In nearby late-stage mergers, an AGN is encapsulated by obscuring material with a column density of $N_H > 10^{23} \text{ cm}^{-2}$, which covers almost the entire circumference of the X-ray

source⁴³. In addition, about 30% of AGNs detected with hard X-rays have a column density of $N_H > 10^{24-25} \text{ cm}^{-2}$ (ref. 44). The fraction of obscured AGN increases to 50% at $z \approx 3$ (ref. 45). Cosmological simulations also predict that there are more dust-obscured quasars in the early Universe than known optically luminous quasars discovered so far⁴⁶. It is difficult to identify such dust-obscured quasars at high redshift in wide-field surveys at optical and near-infrared wavelengths where dust attenuates the emission.

High-resolution observations of highly excited CO line emission could be useful to identify such dust-obscured quasars even with $N_H \approx 10^{25} \text{ cm}^{-2}$. Figure 6 shows a comparison of the galaxy-integrated CO SLED for J2310+1855 (refs. 9,10) with other optically luminous quasars^{11,47–51} and dusty star-forming galaxies^{52–56}. J2310+1855 is among the brightest unobscured quasars at $z = 6$ –7 in terms of CO luminosity. Although there is no noticeable difference in the shape of the CO SLED between J2310+1855 and CO-faint quasars, we cannot conclude from the observation of this single object that X-ray-heated gas is present in the centres of all quasars. Meanwhile, similarly bright high- J CO line emissions have been detected in dusty star-forming galaxies at $z = 4$ –7. The CO luminosity of these objects remains strong even at $J_{\text{up}} = 9$ –10, suggesting the possible presence of an X-ray source such as an AGN at their centres. Hot dust-obscured galaxies with bolometric luminosities of $L_{\text{bol}} > 10^{14} L_\odot$ are also good candidates for extremely dust-obscured quasars, because their SEDs suggest the existence of hot dust with a temperature of about 450 K (ref. 57). Future high-resolution observations with ALMA will allow us to probe the warm gas in the centres of dusty star-forming galaxies and hot dust-obscured galaxies and to study their excitation mechanisms. As shown in Fig. 2, the measured luminosity ratio of $L_{\text{CO}(14-13)}/L_{\text{CO}(13-12)}$ allows us to rule out the possibility of gas heating by a starburst with high SFRs. These candidates of dust-obscured quasars may be at a different evolutionary stage than unobscured quasars where strong AGN-driven outflows have removed the surrounding obscuring material. In this case, only XDR heating would dominate the excitation of high- J CO emission lines, so that, in contrast to J2310+1855, the CO line ratio would be expected to decrease monotonically from the centre to the outer region. James Webb Space Telescope observations are also finding a new population of less luminous AGN candidates with a dusty core at $z > 4$ (refs. 58,59). A complete study of quasars in different phases,

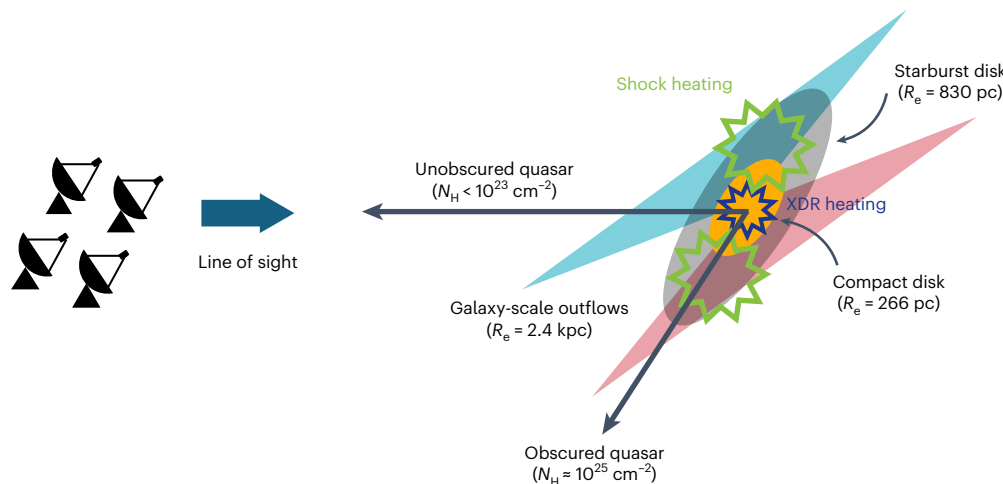


Fig. 5 | Schematic view of J2310+1855. This figure illustrates the composition of the quasar, which consists of a compact disk, a starburst disk and an outflow component. It shows that XDR heating dominates as the heating mechanism in the central region of the quasar, whereas shock heating becomes dominant in regions slightly farther away.

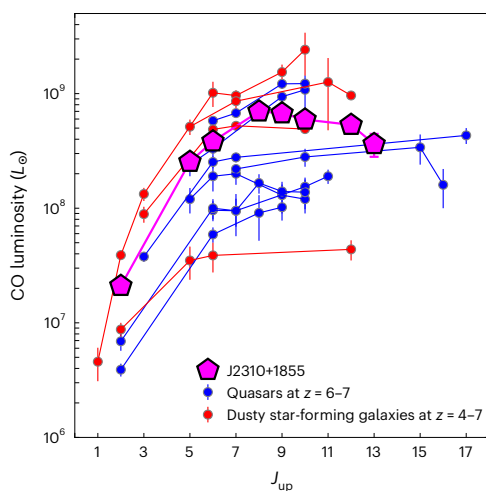


Fig. 6 | Galaxy-integrated CO SLEDs. The magenta pentagon, blue circles and red squares represent J2310+1855, optically luminous quasars at $z = 6-7$ (refs. 8,10,11,47–51) and dusty star-forming galaxies at $z = 4-7$ (refs. 52–56). The error bars represent 1σ uncertainties of the flux measurements.

including extremely dust-obscured ones, is important for a comprehensive understanding of their evolution.

Methods

Sample

Quasar J2310+1855 was first identified by the Sloan Digital Sky Survey¹², and its spectroscopic redshift at $z = 6.003$ was precisely measured by ALMA observations of [CII] line emission⁶. It is one of the brightest quasars at $z > 6$, with a bolometric luminosity of $L_{\text{bol}} = 7.1 \times 10^{13} L_{\odot}$, based on an absolute magnitude at rest-frame 1,450 Å (ref. 30) and a far-infrared luminosity of $L_{\text{FIR}} = (1.4-1.6) \times 10^{13} L_{\odot}$ (ref. 25). In addition, X-ray emission attributed to an accreting SMBH was observed by Chandra, with a luminosity of $L_{2-10\text{keV}} = 1.8 \times 10^{41} \text{ erg s}^{-1}$ in the rest-frame 2–10 keV band³⁰. The mass of the black hole is calculated to be in the range of $M_{\text{BH}} = (2-4) \times 10^9 M_{\odot}$, inferred from the broad MgII emission line¹³. Extended Data Fig. 1 compares the black hole mass and bolometric luminosity of J2310+1855 with those of other quasars. The Eddington ratio, which compares the bolometric luminosity with the theoretical maximum luminosity, of J2310+1855 is close to 1, suggesting that the gas accretion rate to the black hole is higher than that of most quasars

discovered in this epoch. In this study, we spatially resolve the CO emission with a high spatial resolution to investigate the properties of the interstellar medium in the vicinity of a SMBH.

ALMA Data

In J2310+1855, we made new observations of CO ($J = 6-5$), CO ($J = 8-7$), CO ($J = 13-12$), CO ($J = 14-13$) and [CII] line and dust continuum emissions by using ALMA (2019.1.00080.S and 2022.1.01473.S). For a [CII] line, we additionally used datasets from the ALMA archive (2019.1.01721.S, 2018.1.00597.S and 2019.1.00661.S). The used receivers, baseline lengths, maximum recovery scale and integration time are summarized in Extended Data Table 1. At $z = 6.00$, both CO ($J = 13-12$) and CO ($J = 14-13$) emissions were observed simultaneously with a single-frequency set-up. The wavelengths of the dust continuum emissions are 3.5 mm, 3.1 mm, 2.3 mm, 2.1 mm, 1.4 mm, 1.1 mm and 450 μm in the observed frame, corresponding to 499, 437, 328, 301, 193, 162 and 64 μm in the rest frame. Because the maximum recovery scale of the observations of CO ($J = 13-12$), CO ($J = 14-13$) and 1.4 mm continuum emissions is 0.86'' (4.9 kpc), we do not discuss the total fluxes of these emissions in this Article. We use the Common Astronomy Software Application (CASA) package⁶⁰ for the data calibration. We first estimated the continuum flux densities with a first-order polynomial in the frequency range where emission lines are not included and then subtracted them from the visibility data by using CASA/uvcontsub task.

For CO line emissions, we collapsed the visibility data in the velocity range from -150 km s^{-1} to $+150 \text{ km s}^{-1}$ and in the velocity range from -250 km s^{-1} to $+250 \text{ km s}^{-1}$ to increase the signal-to-noise ratio for deconvolution in imaging processing. We then adjusted the visibility weight with Briggs weight to create images with different spatial resolutions from $0.028'' \times 0.018''$ to $0.24'' \times 0.24''$ by using CASA/tclean task and CASA/imsMOOTH task, which smooths images to an arbitrary beam. We cleaned down to the 1.5σ noise level in a circular mask. For a [CII] line, we created a dirty cube with a velocity width of 30 km s^{-1} from all archival data. The synthesized beam size, imaging parameters (radius of circular mask, robustness parameter for Briggs weighting and full width at half maximum of a Gaussian taper) and noise level of these images are summarized in Extended Data Table 2. Extended Data Figs. 4 and 5 show the ALMA images of dust continuum emission and CO line emission, respectively. We took the peak values on the 0.08''-resolution and the 0.24''-resolution images, corresponding to the fluxes or flux densities in the central and extended regions, respectively (Extended Data Table 3). We then calculated the CO fluxes in the outer region at $R = 230-700 \text{ pc}$ by subtracting those at 0.08'' resolution from those

at 0.24'' resolution. These fluxes or flux densities are used to study CO SLEDs and dust SEDs (Fig. 3).

Disk modelling in the visibility plane

Extended Data Fig. 2 shows the ALMA images of the 1.4-mm continuum emission. For the disk modelling, we do not use the ALMA images, but the visibility data. The model has an exponential profile with six parameters (central position, flux density, effective radius, major-to-minor axis ratio and position angle). We fit one- and two-component models to the ALMA data by using the UVMULTIFIT code⁶¹. We then made dirty images after subtracting the best-fit model in the visibility plane. In the one-component model, we obtained a flux density of $S = 4.98 \pm 0.04$ mJy, an effective radius of $R_e = 0.087'' \pm 0.001''$, an axis ratio of $q = 0.74 \pm 0.01$ and a position angle of $PA = -41 \pm 2^\circ$. We found that there is residual emission above 10σ in the centre (Extended Data Fig. 2). In the two-component model, we obtained $S = 1.72 \pm 0.15$ mJy, $R_e = 0.047'' \pm 0.006''$ ($R_e = 266 \pm 14$ pc), $q = 0.63 \pm 0.03$ and $PA = -35 \pm 3^\circ$ for the compact disk and $S = 4.06 \pm 0.13$ mJy, $R_e = 0.145'' \pm 0.003''$ ($R_e = 830 \pm 36$ pc), $q = 0.79 \pm 0.02$ and $PA = -42 \pm 4^\circ$ for the extended disk. There is a small spatial offset of $0.012'' \pm 0.002''$ between the central positions of the two components. The overall emission is well characterized by the two-component model, although off-centre clumps are detected at $6-7\sigma$. The compact disk with $R_e = 266$ pc is roughly comparable in size to a circum-nuclear disk or ring found in nearby AGNs⁶²⁻⁶⁴. The compact disk detected by our ALMA observations could be a circum-nuclear-disk-like component that plays a crucial role as a major reservoir of gas feeding a SMBH. The compact disk contributes about 30% of the total dust emission. Although compact dust emission has been detected in four other quasars at $z = 6-7$ (refs. 16–19), three of them do not exhibit similarly high Eddington ratios (Extended Data Fig. 1). Therefore, it appears that the presence of a compact disk is not limited to phases of high gas accretion rates onto the black hole. Meanwhile, the size of the extended disk with $R_e = 830$ pc is comparable to that of a starburst disk/ring in nearby AGNs⁶³ (about 1 kpc).

We also modelled the wing component ($-465 \text{ km s}^{-1} < \nu < -345 \text{ km s}^{-1}$) and the disk component ($-315 \text{ km s}^{-1} < \nu < +315 \text{ km s}^{-1}$) of the [CII] line emission by using all the archival data. Extended Data Fig. 6 shows the visibility amplitudes of [CII] emission as a function of antenna separation, specifically uv distance in the visibility plane. The wing component decreases steeply at uv distances larger than 100 kλ, indicating that it is spatially extended. The failure to detect the wing component in one of the previous observations³⁶ (2018.1.00597.S) may be due to insufficient sensitivity at short uv distances (<100 kλ). We assumed a circular Gaussian for the wing component and an elliptical exponential disk for the disk component. The best-fit model gives $S_{\text{dv}} = 0.170 \pm 0.021 \text{ Jy km s}^{-1}$ and $R_e = 0.42'' \pm 0.07''$ for the wing component (Extended Data Fig. 6) and $S_{\text{dv}} = 7.85 \pm 0.05 \text{ Jy km s}^{-1}$, $R_e = 0.28'' \pm 0.01''$, $q = 0.70 \pm 0.02$ and $PA = 322 \pm 2^\circ$ for the disk component. The circularized effective radius of the disk component is $R_{e,\text{circ}} = 0.23'' \pm 0.01''$. This value is slightly larger than that reported in a previous image-based analysis ($R_{e,\text{circ}} = 0.19''$ (ref. 26); 2019.1.00661.S and 2019.1.01721.S), but this is probably due to differences in measurement methods and datasets. We derived $R_{e,\text{circ}} = 0.20'' \pm 0.01''$ by fitting only the same visibility data from 2019.1.00661.S to an elliptical exponential disk model.

PDR and XDR model

We used the galaxySLED code to produce model CO SLEDs²⁴. Although many theoretical models assume a constant gas density, our model considers giant molecular clouds (GMCs), which are composed of molecular clumps with different gas densities. The clump density distribution within a GMC follows a log-normal distribution, and 15 types of GMC with different masses and sizes are available in galaxySLED. We distributed the 15 GMCs to create an exponential disk model with a scale length of $R_d = R_e/1.68$ and a total gas mass of M_{gas} .

We assumed a thick disk with a ratio of scale height to radial scale length of $q = z_d/R_d = 0.3$ (ref. 65).

We consider a situation where there is an AGN with X-ray luminosity L_X at the centre of the gas disk. The incident X-ray flux $F_X(r)$ at a distance r from the centre depends on the radial gas column density, because it is attenuated by the gas in the disk. Therefore, in a gas disk characterized by three parameters M_{gas} , R_d and q , we calculated the average radial column density as

$$N_H(r) = \int_0^r \frac{M(x)}{\mu m_p V(x)} dx = \frac{2.08 \times 10^4 M_{\text{gas}}}{\mu m_p} \int_0^r \frac{1 - \exp(-x/R_d)(x/R_d + 1)}{2\pi q R_d x^2} dx,$$

where μ is the mean molecular weight and m_p is the mass of a proton. In J2310+1855, we know that $R_e = 266$ pc from the ALMA observations of 1.4-mm continuum emission and $L_{2-10\text{keV}} = 6.9 \times 10^{44} \text{ erg s}^{-1}$ from X-ray observations³⁰. Although M_{gas} is the only free parameter in our model, the fundamentally important physical parameter contributing to X-ray attenuation is the gas column density. Because the gas mass and the disk thickness are degenerate for a given gas column density, we do not use the gas mass for discussion in this work. In Extended Data Fig. 3, we show the gas column densities and X-ray fluxes at different galactocentric radii in three models with different gas masses of $M_{\text{gas}} = 10^{9,24,9.74,10.24} M_\odot$. In these models, the gas column densities reach $N_H(r = 1 \text{ kpc}) = 10^{24,5.25,0.25,5} \text{ cm}^{-2}$ at a galactocentric radius of 1 kpc. In each GMC distributed at different galactocentric radii in the gas disk, the CO fluxes are calculated using the photoionization code CLOUDY⁶⁶ under different incident X-ray flux conditions. The temperature of the warm gas in J2310+1855 is estimated to be above 200 K (ref. 10). At $z = 6$, the cosmic microwave background temperature is 18 K, which substantially affects the excitation states of cold gas below 100 K (ref. 67). However, the cosmic microwave background should have little impact on warm gas above 200 K. As the gas column density in the radial direction of the disk increases, CO becomes less excited. In the PDR model, the incident ultraviolet flux does not depend on the galactocentric radius because star formation is assumed to occur throughout the gas disk. The integrated CO flux from these GMCs is used in Fig. 2. In Fig. 3 (right), we normalized the model CO SLEDs to the CO $J = 13-12$ line, as this avoids the need to rely on a CO-to-H₂ conversion factor.

Dust SED

We detected multiwavelength continuum emissions at resolutions of 0.08'' and 0.24'' (Extended Data Fig. 4 and Extended Data Table 3), providing the dust SED in the central region and extended regions, respectively. We used the MERCURIUS code⁶⁸ to fit a modified black-body radiation model to the ALMA dust emission data. The model has four parameters: dust mass M_d (or a total infrared luminosity L_{IR}), dust temperature T_d and an emissivity index β , the wavelength at which the dust optical depth is unity λ_0 . We adopted a self-consistent opacity model where the optical depth is proportional to the surface density of the dust mass. We assumed that dust emission is homogeneously distributed in the synthesized beam and that the area of dust emission is equal to the effective area of the beam (0.236 kpc² and 2.20 kpc²). The 450-μm (rest-frame 64 μm) photometry in band 9 is available only for the SED in the extended region. In addition to the measurement uncertainties, the flux calibration uncertainties of 5% in bands 3 and 4, 10% in band 6 and 20% in band 9 are included in the fitting. The best-fit model gives $M_d = 3.1_{-0.9}^{+1.1} \times 10^8 M_\odot$, $L_{\text{IR}} = 3.8_{-1.0}^{+1.7} \times 10^{12} L_\odot$, $T_d = 74_{-5}^{+7} \text{ K}$, $\beta = 1.7_{-0.2}^{+0.2}$ and $\lambda_0 = 266_{-49}^{+52} \mu\text{m}$ in the central region and $M_d = 7.0_{-1.3}^{+1.7} \times 10^8 M_\odot$, $L_{\text{IR}} = 1.2_{-0.3}^{+0.4} \times 10^{13} L_\odot$, $T_d = 59_{-4}^{+4} \text{ K}$, $\beta = 1.6_{-0.1}^{+0.1}$ and $\lambda_0 = 115_{-13}^{+16} \mu\text{m}$ in the extended region. Previous studies of spatially unresolved dust SED including Herschel photometry (100–500 μm) show average dust temperatures of $T_d = 53 \text{ K}$ (ref. 36) and $T_d = 71 \text{ K}$ (ref. 26). In galaxy-integrated SEDs at 100–350 μm, the contribution

of an AGN torus becomes large. The dust temperature of a cold component is affected by the choice of torus model. In addition, by averaging the dust emission over the entire galaxy, the surface density of the dust mass becomes smaller compared with that in the central region of the galaxy, thus reducing the apparent optical depth. Therefore, it is difficult to directly compare the results of resolved and unresolved dust SEDs.

Dust correction for CO line emission

The correction for dust attenuation of the CO line emission is based on the literature³⁸. This approach assumes that gas and dust are well mixed. As the optical depth of the dust increases, the observed CO flux (F) is attenuated from its intrinsic flux (F_0) according to $F = F_0(1 - \tau_\lambda)/\tau_\lambda$. For observations of low- J CO line emission in normal star-forming galaxies, the dust is optically thin at these wavelengths. However, for observations of high- J CO line in extremely dusty objects such as Arp 220, the optical depth exceeds unity at these wavelengths, requiring an attenuation correction. From the dust SED of J2310+1855 shown in Fig. 3 (left), we find that the wavelength at which the dust optical depth reaches unity is $\lambda_0 = 266 \mu\text{m}$ and the wavelength dependence of the optical depth is $\tau_\lambda = (\lambda/\lambda_0)^{-1.7}$. Therefore, the correction factor (F_0/F) becomes 1.2, 1.4, 2.0 and 2.2 at the wavelengths of the CO $J = 6-5$, $J = 8-7$, $J = 13-12$ and $J = 14-13$ line, respectively.

Data availability

All the ALMA data are publicly available via the ALMA archive at <https://almascience.nao.ac.jp/daq/>, with the programme IDs ADS/JAO.ALMA#2018.1.00597.S, ADS/JAO.ALMA#2019.1.00080.S, ADS/JAO.ALMA#2019.1.00661.S, ADS/JAO.ALMA#2019.1.01721.S and ADS/JAO.ALMA#2022.1.01473.S (see also Extended Data Table 1).

Code availability

The codes used in the data analysis (CASA, UVMULTIFIT, galaxySLED and MERCURIUS) are all publicly available.

References

- Mortlock, D. J. et al. A luminous quasar at a redshift of $z = 7.085$. *Nature* **474**, 616–619 (2011).
- Matsuoka, Y. et al. Subaru high- z exploration of low-luminosity quasars (SHELLQs). V. Quasar luminosity function and contribution to cosmic reionization at $z = 6$. *Astrophys. J.* **869**, 150 (2018).
- Onoue, M. et al. Subaru high- z exploration of low-luminosity quasars (SHELLQs). VI. Black hole mass measurements of six quasars at $6.1 \leq z \leq 6.7$. *Astrophys. J.* **880**, 77 (2019).
- Yang, J. et al. Probing early supermassive black hole growth and quasar evolution with near-infrared spectroscopy of 37 reionization-era quasars at $6.3 < z \leq 7.64$. *Astrophys. J.* **923**, 262 (2021).
- Bertoldi, F. et al. Dust emission from the most distant quasars. *Astron. Astrophys.* **406**, L55–L58 (2003).
- Wang, R. et al. Star formation and gas kinematics of quasar host galaxies at $z \sim 6$: new insights from ALMA. *Astrophys. J.* **773**, 44 (2013).
- Davies, R. I. et al. Fueling active galactic nuclei. II. Spatially resolved molecular inflows and outflows. *Astrophys. J.* **792**, 101 (2014).
- Gallerani, S. et al. First CO(17–16) emission line detected in a $z > 6$ quasar. *Mon. Not. R. Astron. Soc.* **445**, 2848–2853 (2014).
- Carniani, S. et al. Constraints on high- J CO emission lines in $z \sim 6$ quasars. *Mon. Not. R. Astron. Soc.* **489**, 3939–3952 (2019).
- Li, J. et al. Probing the full CO spectral line energy distribution (SLED) in the nuclear region of a quasar-starburst system at $z = 6.003$. *Astrophys. J.* **889**, 162 (2020).
- Pensabene, A. et al. ALMA multiline survey of the ISM in two quasar host-companion galaxy pairs at $z > 6$. *Astron. Astrophys.* **652**, A66 (2021).
- Jiang, L. et al. The final SDSS high-redshift quasar sample of 52 quasars at $z > 5.7$. *Astrophys. J.* **833**, 222 (2016).
- Farina, E. P. et al. The X-shooter/ALMA sample of quasars in the epoch of reionization. II. Black hole masses, Eddington ratios, and the formation of the first quasars. *Astrophys. J.* **941**, 106 (2022).
- Xu, C. K. et al. ALMA Observations of Warm Molecular Gas and Cold Dust in NGC 34. *Astrophys. J.* **787**, 48 (2014).
- Xu, C. K. et al. ALMA observations of warm dense gas in NGC 1614—breaking of the star formation law in the central kiloparsec. *Astrophys. J.* **799**, 11 (2015).
- Venemans, B. P. et al. 400 pc imaging of a massive quasar host galaxy at a redshift of 6.6. *Astrophys. J.* **874**, L30 (2019).
- Walter, F. et al. ALMA 200 pc imaging of a $z \sim 7$ quasar reveals a compact, disk-like host galaxy. *Astrophys. J.* **927**, 21 (2022).
- Meyer, R. A. et al. ALMA 300 pc resolution imaging of a $z = 6.79$ Quasar: no evidence for supermassive black hole influence on the CII kinematics. *Astrophys. J.* **956**, 127 (2023).
- Neeleman, M. et al. ALMA 400 pc imaging of a $z = 6.5$ massive warped disk galaxy. *Astrophys. J.* **958**, 132 (2023).
- van der Werf, P. P. et al. Black hole accretion and star formation as drivers of gas excitation and chemistry in Markarian 231. *Astron. Astrophys.* **518**, L42 (2010).
- Mashian, N. et al. High- J CO SLEDs in nearby infrared bright galaxies observed by Herschel/PACS. *Astrophys. J.* **802**, 81 (2015).
- Meijerink, R. et al. Evidence for CO shock excitation in NGC 6240 from Herschel SPIRE spectroscopy. *Astrophys. J.* **762**, L16 (2013).
- Vallini, L. et al. Impact of X-rays on CO emission from high- z galaxies. *Mon. Not. R. Astron. Soc.* **490**, 4502–4514 (2019).
- Esposito, F. et al. Modelling molecular clouds and CO excitation in AGN-host galaxies. *Mon. Not. R. Astron. Soc.* **527**, 8727–8745 (2024).
- Shao, Y. et al. Star formation and ISM properties in the host galaxies of three far-infrared luminous quasars at $z \sim 6$. *Astrophys. J.* **876**, 99 (2019).
- Tripodi, R. et al. Black hole and host galaxy growth in an isolated $z \sim 6$ QSO observed with ALMA. *Astron. Astrophys.* **665**, A107 (2022).
- Esposito, F. et al. AGN impact on the molecular gas in galactic centres as probed by CO lines. *Mon. Not. R. Astron. Soc.* **512**, 686–711 (2022).
- Vallini, L. et al. Molecular cloud photoevaporation and far-infrared line emission. *Mon. Not. R. Astron. Soc.* **467**, 1300–1312 (2017).
- Mingozi, M. et al. CO excitation in the Seyfert galaxy NGC 34: stars, shock or AGN driven? *Mon. Not. R. Astron. Soc.* **474**, 3640–3648 (2018).
- Vito, F. et al. The X-ray properties of $z > 6$ quasars: no evident evolution of accretion physics in the first Gyr of the Universe. *Astron. Astrophys.* **630**, A118 (2019).
- Bischetti, M. et al. Widespread QSO-driven outflows in the early Universe. *Astron. Astrophys.* **630**, A59 (2019).
- Izumi, T. et al. Subaru high- z exploration of low-luminosity quasars (SHELLQs). XIII. Large-scale feedback and star formation in a low-luminosity quasar at $z = 7.07$ on the local black hole to host mass relation. *Astrophys. J.* **914**, 36 (2021).
- Flower, D. R. & Pineau des Forêts, G. Excitation and emission of H_2 , CO and H_2O molecules in interstellar shock waves. *Mon. Not. R. Astron. Soc.* **406**, 1745–1758 (2010).
- Flower, D. R. & Pineau des Forêts, G. Interpreting observations of molecular outflow sources: the MHD shock code mhd_vode. *Astron. Astrophys.* **578**, A63 (2015).
- Gonzalez-Alfonso, E. et al. Herschel observations of water vapour in Markarian 231. *Astron. Astrophys.* **518**, L43 (2010).
- Shao, Y. et al. The interstellar medium distribution, gas kinematics, and system dynamics of the far-infrared luminous quasar SDSS J2310+1855 at $z = 6.0$. *Astron. Astrophys.* **668**, A121 (2022).

37. Tsukui, T., Wisnioski, E., Krumholz, M. R. & Battisti, A. Spatially resolved dust properties and quasar-galaxy decomposition of a hyper-luminous infrared galaxy at $z = 4.4$. *Mon. Not. R. Astron. Soc.* **523**, 4654–4679 (2023).
38. Rangwala, N. et al. Observations of Arp 220 using Herschel-SPIRE: an unprecedented view of the molecular gas in an extreme star formation environment. *Astrophys. J.* **743**, 94 (2011).
39. Tripodi, R. et al. Dynamical signature of a stellar bulge in a quasar-host galaxy at $z \approx 6$. *Astron. Astrophys.* **671**, A44 (2023).
40. Saito, T. et al. AGN-driven cold gas outflow of NGC 1068 characterized by dissociation-sensitive molecules. *Astrophys. J.* **935**, 155 (2022).
41. Vayner, A. et al. First results from the JWST early release science program Q3D: ionization cone, clumpy star formation, and shocks in a $z = 3$ extremely red quasar host. *Astrophys. J.* **955**, 92 (2023).
42. Hopkins, P. F. et al. A unified, merger-driven model of the origin of starbursts, quasars, the cosmic X-ray background, supermassive black holes, and galaxy spheroids. *Astrophys. J. Suppl. Ser.* **163**, 1–49 (2006).
43. Ricci, C. et al. Growing supermassive black holes in the late stages of galaxy mergers are heavily obscured. *Mon. Not. R. Astron. Soc.* **468**, 1273–1299 (2017).
44. Ricci, C. et al. Compton-thick accretion in the local Universe. *Astrophys. J.* **815**, L13 (2015).
45. Lanzuisi, G. et al. The Chandra COSMOS Legacy Survey: Compton thick AGN at high redshift. *Mon. Not. R. Astron. Soc.* **480**, 2578–2592 (2018).
46. Ni, Y. et al. QSO obscuration at high redshift ($z \gtrsim 7$): predictions from the BLUETIDES simulation. *Mon. Not. R. Astron. Soc.* **495**, 2135–2151 (2020).
47. Riechers, D. A. et al. Imaging atomic and highly excited molecular gas in a $z = 6.42$ quasar host galaxy: copious fuel for an eddington-limited starburst at the end of cosmic reionization. *Astrophys. J.* **703**, 1338–1345 (2009).
48. Wang, F. et al. Spatially resolved interstellar medium and highly excited dense molecular gas in the most luminous quasar at $z = 6.327$. *Astrophys. J.* **880**, 2 (2019).
49. Yang, J. et al. Far-infrared properties of the bright, gravitationally lensed quasar J0439+1634 at $z = 6.5$. *Astrophys. J.* **880**, 153 (2019).
50. Li, J. et al. Diverse molecular gas excitations in quasar host galaxies at $z \sim 6$. *Astrophys. J.* **962**, 119 (2024).
51. Xu, F. et al. Constraining the excitation of molecular gas in two quasar-starburst systems at $z \sim 6$. *Astrophys. J.* **977**, 190 (2024).
52. Riechers, D. A. et al. A dust-obscured massive maximum-starburst galaxy at a redshift of 6.34. *Nature* **496**, 329–333 (2013).
53. Salomé, P. et al. BR1202–0725: an extreme multiple merger at $z = 4.7$. *Astron. Astrophys.* **545**, A57 (2012).
54. Lee, M. M. et al. Dense and warm neutral gas in BR 1202–0725 at $z = 4.7$ as traced by the [O I] 145 μm line. *Astrophys. J.* **913**, 41 (2021).
55. Jarugula, S. et al. Molecular line observations in two dusty star-forming galaxies at $z = 6.9$. *Astrophys. J.* **921**, 97 (2021).
56. Tsujita, A. et al. Central concentration of warm and dense molecular gas in a strongly lensed submillimeter galaxy at $z = 6$. *Publ. Astron. Soc. Jpn* **74**, 1429–1440 (2022).
57. Tsai, C.-W. et al. The most luminous galaxies discovered by WISE. *Astrophys. J.* **805**, 90 (2015).
58. Matthee, J. et al. Little red dots: an abundant population of faint active galactic nuclei at $z \sim 5$ revealed by the EIGER and FRESCO JWST surveys. *Astrophys. J.* **963**, 129 (2024).
59. Barro, G. et al. Extremely red galaxies at $z = 5$ –9 with MIRI and NIRSpec: dusty galaxies or obscured active galactic nuclei? *Astrophys. J.* **963**, 128 (2024).
60. CASA Team CASA, the common astronomy software applications for radio astronomy. *Publ. Astron. Soc. Pacif.* **134**, 114501 (2022).
61. Martí-Vidal, I., Vlemmings, W. H. T., Muller, S. & Casey, S. UVMULTIFIT: a versatile tool for fitting astronomical radio interferometric data. *Astron. Astrophys.* **563**, A136 (2014).
62. Izumi, T. et al. Submillimeter ALMA observations of the dense gas in the low-luminosity type-1 active nucleus of NGC 1097. *Publ. Astron. Soc. Jpn* **65**, 100 (2013).
63. García-Burillo, S. et al. Molecular line emission in NGC 1068 imaged with ALMA. I. An AGN-driven outflow in the dense molecular gas. *Astron. Astrophys.* **567**, A125 (2014).
64. Combes, F. et al. ALMA reveals the feeding of the Seyfert 1 nucleus in NGC 1566. *Astron. Astrophys.* **565**, A97 (2014).
65. Sani, E. et al. Physical properties of dense molecular gas in centres of Seyfert galaxies. *Mon. Not. R. Astron. Soc.* **424**, 1963–1976 (2012).
66. Ferland, G. J. et al. The 2017 Release Cloudy. *Rev. Mex. Astron. Astrofis.* **53**, 385–438 (2017).
67. da Cunha, E. et al. On the effect of the cosmic microwave background in high-redshift (sub-)millimeter observations. *Astrophys. J.* **766**, 13 (2013).
68. Witstok, J. et al. Dual constraints with ALMA: new [O III] 88- μm and dust-continuum observations reveal the ISM conditions of luminous LBGs at $z \sim 7$. *Mon. Not. R. Astron. Soc.* **515**, 1751–1773 (2022).

Acknowledgements

This Article makes use of the following ALMA data: ADS/JAO.ALMA#2018.1.00597.S, ADS/JAO.ALMA#2019.1.00080.S, ADS/JAO.ALMA#2019.1.00661.S, ADS/JAO.ALMA#2019.1.01721.S and ADS/JAO.ALMA#2022.1.01473.S. ALMA is a partnership of ESO (representing its member states), NSF (USA) and NINS (Japan), together with NRC (Canada), NSTC and ASIAA (Taiwan) and KASI (Republic of Korea), in cooperation with the Republic of Chile. The Joint ALMA Observatory is operated by ESO, AUI/NRAO and NAOJ. K.T. acknowledges support from JSPS KAKENHI grant numbers JP 23K03466 and 23K20870. F.E. acknowledges support from grant PRIN MIUR 2017-20173ML3WW_s and funding from the INAF Mini Grant 2022 programme ‘Face-to-Face with the Local Universe: ISM’s Empowerment (LOCAL)’. T.M. is supported by a University Research Support Grant from the National Astronomical Observatory of Japan (NAOJ). K.T. was supported by the ALMA Japan Research Grant of NAOJ ALMA Project, NAOJ-ALMA-354. Data analysis was in part carried out on the Multi-wavelength Data Analysis System operated by the Astronomy Data Center (ADC), National Astronomical Observatory of Japan.

Author contributions

K.T. led the project and reduced the ALMA data. F.E. and L.V. supported the modelling of the CO emission and helped in the interpretation of the results. All other authors contributed to the interpretation of the results and commented on the manuscript and the ALMA proposals.

Competing interests

The authors declare no competing interests.

Additional information

Extended data is available for this paper at <https://doi.org/10.1038/s41550-025-02505-x>.

Correspondence and requests for materials should be addressed to K. Tadaki.

Peer review information *Nature Astronomy* thanks the anonymous reviewers for their contribution to the peer review of this work.

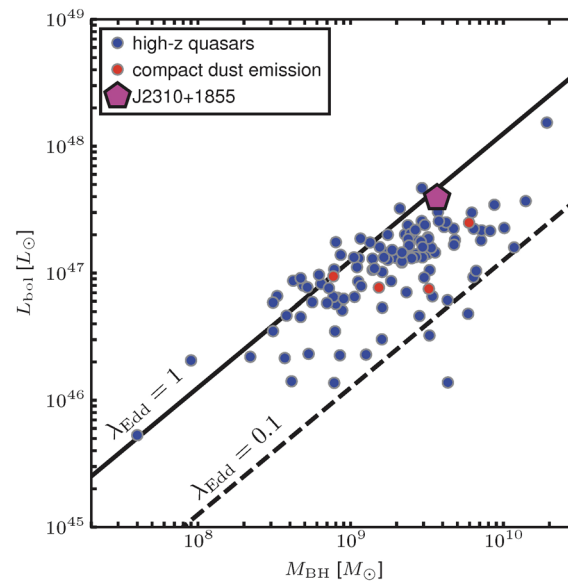
Reprints and permissions information is available at www.nature.com/reprints.

Publisher's note Springer Nature remains neutral with regard to jurisdictional claims in published maps and institutional affiliations.

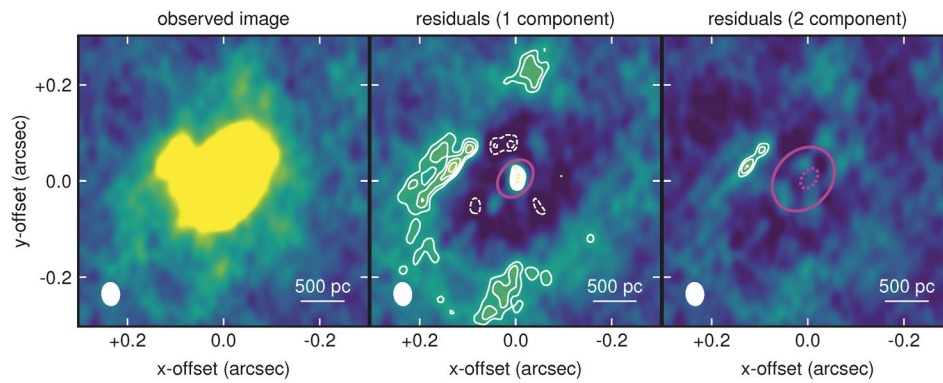
Springer Nature or its licensor (e.g. a society or other partner) holds exclusive rights to this article under a publishing agreement with

the author(s) or other rightsholder(s); author self-archiving of the accepted manuscript version of this article is solely governed by the terms of such publishing agreement and applicable law.

© The Author(s), under exclusive licence to Springer Nature Limited 2025

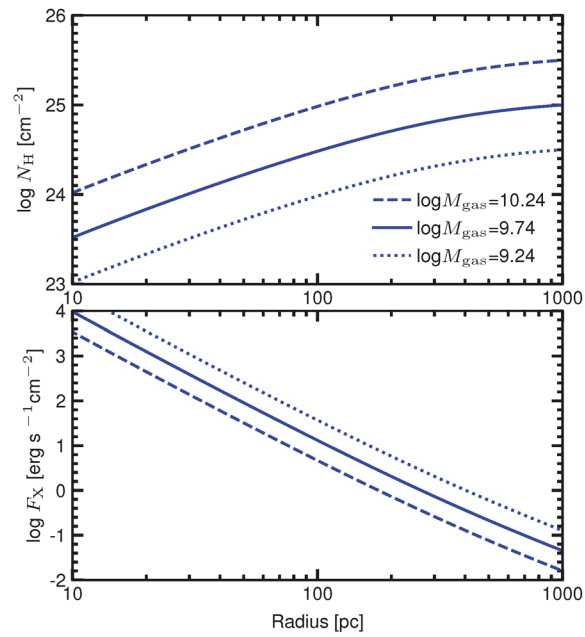


Extended Data Fig. 1 | Black hole mass versus bolometric luminosity for J2310 + 1855 and other quasars at $z \gtrsim 5.7$ ¹³. Red circles indicate quasars where compact dust emission has been detected in high-resolution ALMA observations^{16–19}.

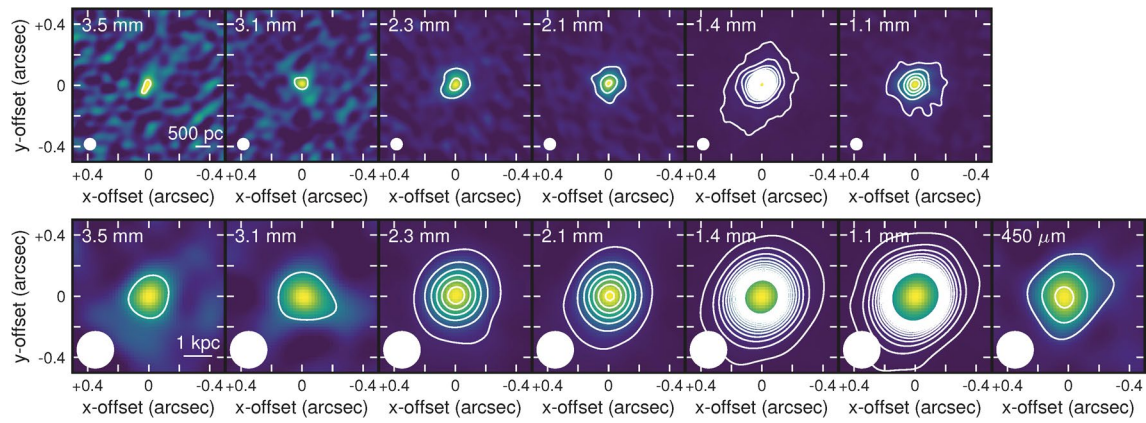


Extended Data Fig. 2 | ALMA images of 1.4 mm continuum emission. From left to right, the observed clean images and the dirty images after subtraction of the best-fit one- and two-component models are shown. The spatial resolution of the

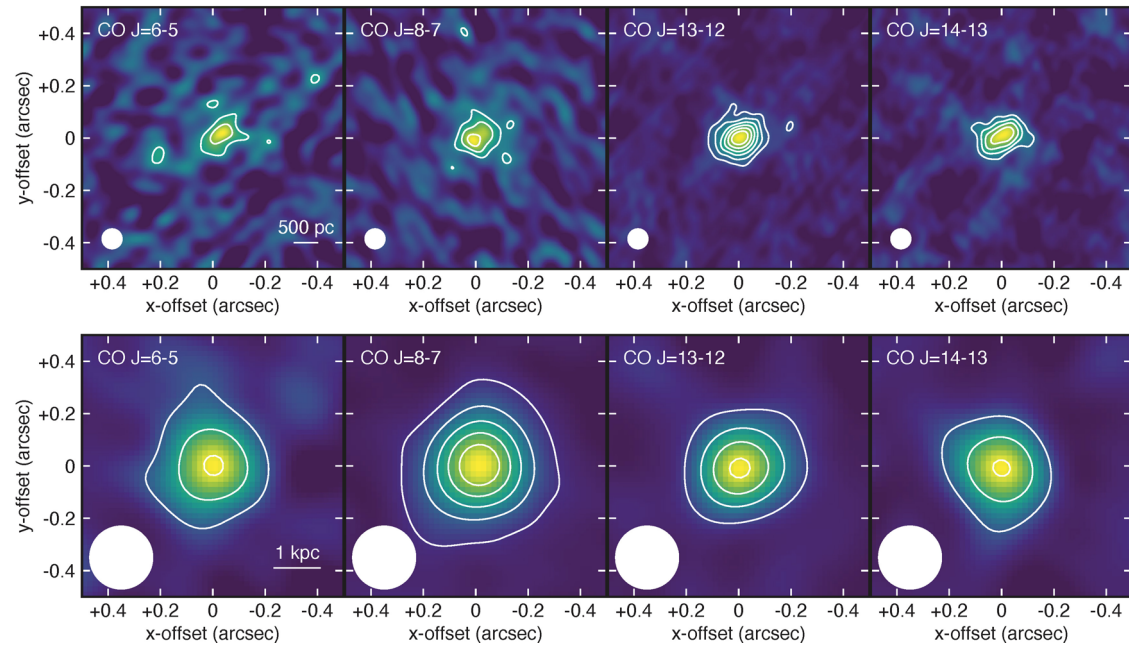
images is $0.050'' \times 0.039''$. Dashed and solid contours are plotted every -1σ from -5σ and every 1σ from 5σ , respectively. The effective radii of the best-fit model are shown by the magenta lines.



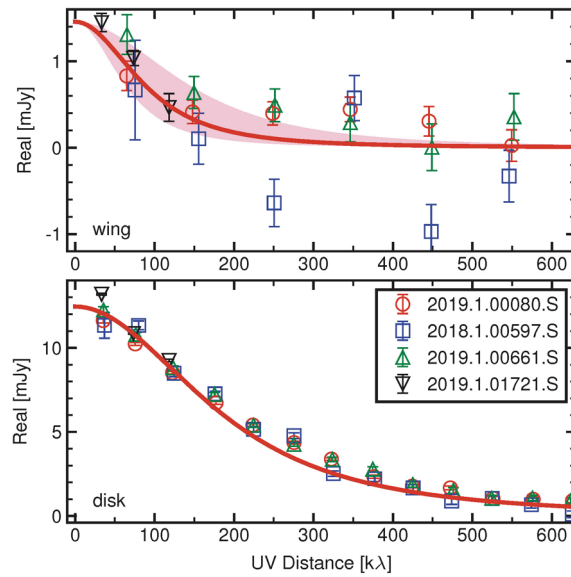
Extended Data Fig. 3 | X-ray-dominated region model. A gas column density (top) and X-ray flux (bottom) at different galactocentric radii. The dotted, solid, and dashed lines show the XDR models with different gas masses.



Extended Data Fig. 4 | ALMA image of dust continuum emission. The beam size is $0.08'' \times 0.08''$ (top) and $0.24'' \times 0.24''$ (bottom). The contours are plotted every 10σ from 5σ .



Extended Data Fig. 5 | ALMA image of CO emission. From left to right, the CO ($J=6-5$), CO ($J=8-7$), CO ($J=13-12$), and CO ($J=14-13$) maps are shown. The beam size is $0.08'' \times 0.08''$ (top) and $0.24'' \times 0.24''$ (bottom). The contours are plotted every 2σ from 3σ .



Extended Data Fig. 6 | Visibility amplitude of [CII] emission. Top, a wing component in in the velocity range of $-465 \text{ km s}^{-1} < v < -345 \text{ km s}^{-1}$. Bottom, a disk component in in the velocity range of $-315 \text{ km s}^{-1} < v < +315 \text{ km s}^{-1}$. Different symbols show different observations (Extended Data Table 1). We show the real part of the visibility as a function of uv distance along the minor axis,

corresponding to the major axis in the images. The center and length of the error bars represent the mean value of the real part of the visibilities and the 1σ uncertainty. A red line and red shaded region show the best-fit model and its uncertainties, respectively.

Extended Data Table 1 | Summary of ALMA observations

Line/continuum	Receivers	5th-80th percentiles of baselines	Maximum recovery scale	Integration time	Project ID
CO (J=6-5) 3.5 mm continuum 3.1 mm continuum	ALMA/Band-3	565 m - 6.2 km	1.2"	45 min	2022.1.01473.S (PI: K. Tadaki)
CO (J=8-7) 2.3 mm continuum 2.1 mm continuum	ALMA/Band-4	344 m - 4.0 km	1.4"	90 min	2022.1.01473.S (PI: K. Tadaki)
CO (J=13-12) CO (J=14-13) 1.4 mm continuum	ALMA/Band-6	338 m - 5.1 km	0.86"	222 min	2019.1.00080.S (PI: K. Tadaki)
[CII] 1.1 mm continuum	ALMA/Band-6	20 m - 0.1 km	12"	135 min	2019.1.01721.S (PI: M. Rafelski)
		144 m - 1.4 km	1.6"	40 min	2018.1.00597.S (PI: Y. Shao)
		75 m - 0.9 km	3.2"	89 min	2019.1.00080.S (PI: K. Tadaki)
		72 m - 0.9 km	3.8"	257 min	2019.1.00661.S (PI: C. Feruglio)
450 μ m continuum	ALMA/Band-9	28 m - 0.2 km	3.3"	19 min	2022.1.01473.S (PI: K. Tadaki)

Observation details for each emission line and continuum emission, including the receiver, baseline lengths encompassing 5% and 80% of all baselines, maximum recovery scale, integration time, and project ID.

Extended Data Table 2 | Summary of image processing

Line/continuum	Beam size	Radius of a circular mask	Robustness parameter	Taper	Velocity width	Noise level
CO (J=6-5)	0.08"×0.08"	0.2"	0.3	-	300 km s ⁻¹	92 μJy
	0.24"×0.24"	0.5"	2	0.13"	500 km s ⁻¹	92 μJy
CO (J=8-7)	0.08"×0.08"	0.2"	-0.15	-	300 km s ⁻¹	73 μJy
	0.24"×0.24"	0.5"	2	0.1"	500 km s ⁻¹	51 μJy
CO (J=13-12) CO (J=14-13)	0.051"×0.039"	0.2"	2	-	300 km s ⁻¹	30 μJy
	0.08"×0.08"	0.2"	2	0.03"	300 km s ⁻¹	32 μJy
	0.24"×0.24"	0.5"	2	0.17"	500 km s ⁻¹	52 μJy
[CII] (v<+225 km s ⁻¹)	1.5"×1.4"	-	2	1.0"	30 km s ⁻¹	108 μJy
[CII] (v>+225 km s ⁻¹)	1.5"×1.4"	-	2	1.2"	30 km s ⁻¹	272 μJy
3.5 mm continuum	0.08"×0.08"	0.2"	0	-	-	18 μJy
	0.24"×0.24"	0.5"	2	0.12"	-	16 μJy
3.1 mm continuum	0.08"×0.08"	0.2"	0.3	-	-	16 μJy
	0.24"×0.24"	0.5"	2	0.13"	-	19 μJy
2.3 mm continuum	0.08"×0.08"	0.2"	-0.1	-	-	16 μJy
	0.24"×0.24"	0.5"	2	0.1"	-	13 μJy
2.1 mm continuum	0.08"×0.08"	0.2"	0	-	-	14 μJy
	0.24"×0.24"	0.5"	2	0.1"	-	13 μJy
1.4 mm continuum	0.029"×0.019"	0.3"	-0.5	-	-	14 μJy
	0.050"×0.039"	0.3"	2	-	-	6.9 μJy
	0.08"×0.08"	0.2"	2	0.03"	-	19 μJy
	0.24"×0.24"	0.5"	2	0.17"	-	16 μJy
1.1 mm continuum (2018.1.00597.S)	0.08"×0.08"	0.2"	-0.5	-	-	32 μJy
1.1 mm continuum (2019.1.00080.S)	0.24"×0.24"	0.5"	1.2	-	-	15 μJy
450 μm continuum	0.24"×0.24"	0.5"	0.1	-	-	608 μJy

Clean parameters and noise levels used to create images for each emission line and continuum emission.

Extended Data Table 3 | Peak flux/flux densities in the ALMA images

	0.08"×0.08" (central region)	0.24"×0.24" (extended region)
CO ($J=6-5$)	$0.183 \pm 0.028 \text{ Jy km s}^{-1}$	$0.624 \pm 0.046 \text{ Jy km s}^{-1}$
CO ($J=8-7$)	$0.175 \pm 0.023 \text{ Jy km s}^{-1}$	$0.707 \pm 0.026 \text{ Jy km s}^{-1}$
CO ($J=13-12$)	$0.148 \pm 0.010 \text{ Jy km s}^{-1}$	$0.495 \pm 0.026 \text{ Jy km s}^{-1}$
CO ($J=14-13$)	$0.109 \pm 0.010 \text{ Jy km s}^{-1}$	$0.370 \pm 0.028 \text{ Jy km s}^{-1}$
3.5 mm continuum	$100 \pm 18 \text{ } \mu\text{Jy}$	$167 \pm 16 \text{ } \mu\text{Jy}$
3.1 mm continuum	$123 \pm 16 \text{ } \mu\text{Jy}$	$245 \pm 19 \text{ } \mu\text{Jy}$
2.3 mm continuum	$323 \pm 16 \text{ } \mu\text{Jy}$	$770 \pm 13 \text{ } \mu\text{Jy}$
2.1 mm continuum	$384 \pm 14 \text{ } \mu\text{Jy}$	$884 \pm 13 \text{ } \mu\text{Jy}$
1.4 mm continuum	$1.33 \pm 0.01 \text{ mJy}$	$3.37 \pm 0.02 \text{ mJy}$
1.1 mm continuum	$1.68 \pm 0.03 \text{ mJy}$	$4.75 \pm 0.01 \text{ mJy}$
450 μm continuum	-	$16.9 \pm 0.6 \text{ mJy}$

Peak flux densities per beam for each emission line and continuum image at each resolution.